Chinese Chemical Letters 31 (2020) 1000–1003

Contents lists available at ScienceDirect

Chinese Chemical Letters

journal homepage: www.elsevier.com/locate/cclet

Communication

Nanostructured Ni/$Ti_3C_2T_x$ MXene hybrid as cathode for lithium-oxygen battery

Caiying Wen[a], Tianjiao Zhu[a], Xingyu Li[a], Huifeng Li[a,*], Xianqiang Huang[b], Genban Sun[a,*]

[a] Beijing Key Laboratory of Energy Conversion and Storage Materials, College of Chemistry, Beijing Normal University, Beijing 100875, China
[b] Shandong Provincial Key Laboratory of Chemical Energy Storage and Novel Cell Technology, School of Chemistry & Chemical Engineering, Liaocheng University, Liaocheng 252059, China

ARTICLE INFO

Article history:
Received 25 July 2019
Received in revised form 6 September 2019
Accepted 9 September 2019
Available online 18 September 2019

Keywords:
MXene
Nickel
Two-dimensional material
Electronic conductivity
Lithium-oxygen battery

ABSTRACT

Ti_3C_2 belongs to MXenes family, which is a new two-dimensional material and has been applied in many fields. With simple method of hydrothermal and high temperature calcination, nanostructured Ni/$Ti_3C_2T_x$ hybrid was synthesized. The stable layer structure of Ti_3C_2 MXene providing high surface area as well as excellent electronic conductivity are beneficial for deposition and decomposition of discharge product Li_2O_2. Furthermore, possessing special catalytic activity, Ni nanoparticles with size of about 20 nm could accelerate Li_2O_2 breaking down. Taking advantage of two kinds of materials, Ni/$Ti_3C_2T_x$ hybrid as cathode of Li-O_2 battery can achieve a maximal specific capacity of 20,264 mAh/g in 100 mA/g and 10,699 mAh/g in 500 mA/g at the first cycle. This work confirms that the prepared Ni/$Ti_3C_2T_x$ hybrid exhibiting better cycling stability points out a new guideline to improve the electrochemical performance of lithium-oxygen batteries.

Among energy storage system, lithium-oxygen battery is recognized as a possible countermeasure for solving energy shortage because of its high theoretical energy density up to 11,400 Wh/kg, while the poor cyclic property and low kinetic reaction rate of oxygen reduction reaction (ORR) and oxygen evolution reaction (OER) limit its commercial use [1–4].

Many sorts of materials have been utilized as cathodes of Li-O_2 battery to improve battery performance such as commodity carbon black, three dimensional structure graphene and nano-porous non-carbon material [5–8]. As a new 2D material, MXene possesses unique electronic and structure properties with electrochemical stability, good electrical conductivity as well as controllable interlayer spacing for diverse intercalants situated at MXene layers, resulting in high surface area [9–11] and it has been extensively used in different energy storage devices such as lithium-ion battery, lithium-sulfur battery and supercapacitor [12–15].

With the popular price, transition metals have been proved to be suitable catalysts for Li-O_2 battery, which can reduce charge overpotential, catalyze the decomposition of discharge product and improve cycle performance of lithium-oxygen battery [11, 16–20]. Liu *et al.* designed 3D ultralight Ni foam with Ru nanoparticles as active electrocatalysts [21] and Oh *et al.* developed novel mNi-NCNT-MoC-C-embedded microsphere as efficient catalyst [22], both exhibiting excellent Li-O_2 battery property. Herein, we report the synthesized Ni/$Ti_3C_2T_x$ hybrid combining the advantages of MXene and Ni, which makes Ni/$Ti_3C_2T_x$ an excellent cathode material for Li-O_2 battery.

A simple synthetic method was applied to get the target Ni/$Ti_3C_2T_x$ hybrid. As illustrated in Fig. 1a, the Al atoms layers of Ti_3AlC_2 were etched by HF, producing accordion-like $Ti_3C_2T_x$. Afterwards, $Ti_3C_2T_x$ was mixed with $Ni(NO_3)_2{\cdot}6H_2O$ and urea, which were heated at 140 °C. Ultimately, the obtained Ni/$Ti_3C_2T_x$ precursor was kept at 400 °C in protected gas Ar. The characterizations of scanning electronic microscope (SEM) and high-resolution transmission electronic microscope (HRTEM) were employed to analyze the microstructure and morphology of Ni/$Ti_3C_2T_x$ hybrid. As can be seen in Figs. 1b and c, compared with raw material, the interlayered spacing of $Ti_3C_2T_x$ is enlarged after HF-etching. The expanded layer structure of MXene, which provides space for nickel nanoparticles to uniformly load on, has been kept after the treatment with hydrothermal and calcination, exhibited in Fig. 1d. Furthermore, Fig. 1e also draws the same conclusion that Ni nanoparticles were evenly dispersed on the surface of $Ti_3C_2T_x$. HRTEM image of Ni/$Ti_3C_2T_x$ (Fig. 1f) shows that the size of nickel nanoparticles is approximately 20 nm, with lattice fringe constants of 0.2037 nm classified as (111) plane for Ni (JCPDS No. 04-0850). The well fabricated Ni/$Ti_3C_2T_x$ was proved to be good crystallinity by the selected area electron

* Corresponding authors.
E-mail address: lihuifeng@bnu.edu.cn (H. Li).

https://doi.org/10.1016/j.cclet.2019.09.028
1001-8417/

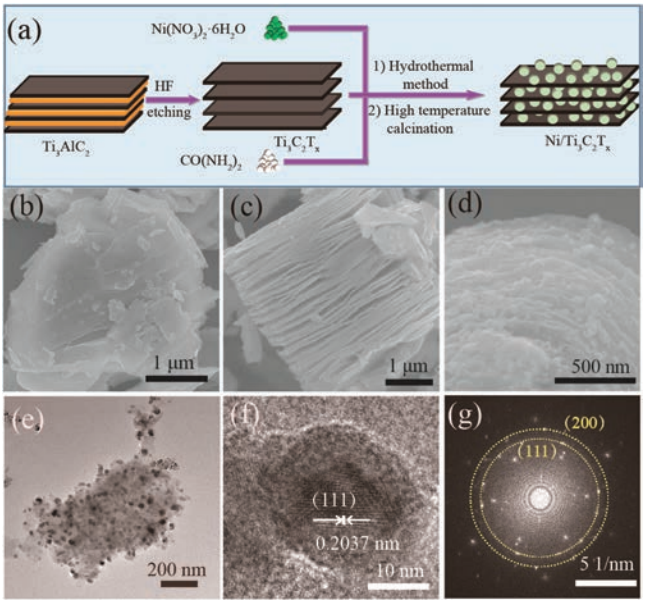

Fig. 1. (a) The schematic diagram of the synthesized method of $Ni/Ti_3C_2T_x$ hybrid, SEM images of (b) Ti_3AlC_2, (c) HF-etching $Ti_3C_2T_x$, (d) $Ni/Ti_3C_2T_x$ hybrid, (e) TEM images of $Ni/Ti_3C_2T_x$ hybrid, (f) HRTEM image of $Ni/Ti_3C_2T_x$. (g) SAED pattern of $Ni/Ti_3C_2T_x$.

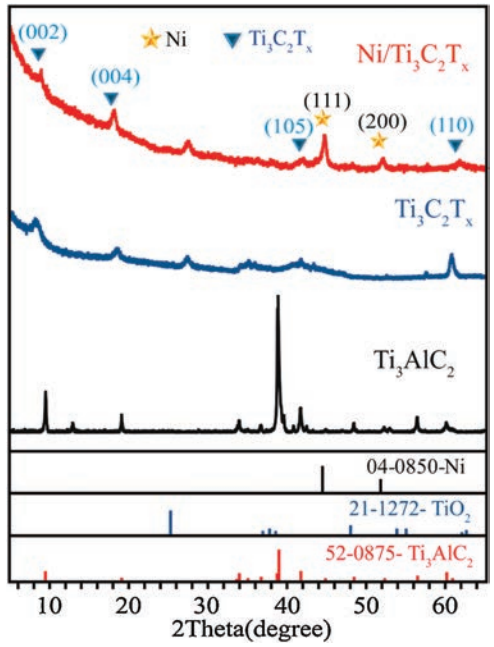

Fig. 2. XRD patterns of Ti_3AlC_2, HF-etching $Ti_3C_2T_x$ and final product $Ni/Ti_3C_2T_x$.

diffraction (SAED) pattern of $Ni/Ti_3C_2T_x$ (Fig. 1g) which demonstrates the single crystal electron diffraction of $Ti_3C_2T_x$ and diffraction circles of Ni consistent with (111) plane and (200) plane of the XRD pattern of Ni. The above characterizations confirm the successful preparation of the $Ni/Ti_3C_2T_x$ hybrid with Ni obtained by pristine Ni^{2+} material experiencing reduction reaction of $Ti_3C_2T_x$. The nanostructured hybrid has special catalytic activity, which contributes to the charge process of lithium-oxygen battery. The energy-dispersive X-ray spectrometer (EDS) is conducted to further elaborate the distribution of Ni on $Ti_3C_2T_x$. As shown in Fig. S1b (Supporting information), nickel nanoparticles uniformly grew on $Ti_3C_2T_x$. The mapping image of F element shows the distribution of similar concentration as Ni, which exhibits the coexistence of fluorine and nickel atoms, implying that some nickel atoms are bonding with fluorine atoms. The concentrations of F and O are appreciable in the entire MXene sheet due to the terminated functional groups, such as —O, —F and —OH. The EDS mapping certifies that the Ni nanoparticles were well-grown on $Ti_3C_2T_x$.

The X-ray diffraction (XRD) is an important characterization to clarify the effect of HF etching and the composition of final product, which is shown in Fig. 2. The peak at 39.0° which represents Al-layered in Ti_3AlC_2 disappeared after HF-etching, proving the removal of Al layer and formation of $Ti_3C_2T_x$. $Ti_3C_2T_x$ has a lot of functional groups which are beneficial for the synthesis of $Ni/Ti_3C_2T_x$. The peaks at 44.5° and 51.8° correspond to (111) and (200) planes of Ni (JCPDS No. 04-0850), indicating that Ni is in the sample. The peak at 41.8° remains in the sample, proving that the structure of $Ti_3C_2T_x$ was not destroyed after high-temperature calcination. No other peaks showed in the XRD pattern, demonstrating that $Ni/Ti_3C_2T_x$ is a pure sample.

To get closer understanding of the chemical state of the nanostructured $Ni/Ti_3C_2T_x$ hybrid, the X-ray photoelectron spectra (XPS) was conducted. As shown in Fig. 3a, the synthesized product was made up of Ni, F, O, Ti and C element. In Fig. 3b, the Ti 2p core level was fitted with three doublets (Ti $2p_{3/2}$-Ti $2p_{1/2}$) with fixed area ratio equal to 2:1. The peaks locating at 455.52 eV, 456.64 eV, 459 eV of Ti $2p_{3/2}$ indicated the presence of Ti-C, Ti^{2+}, Ti-O, separately [23]. Compared to the reported literature [23], these three peaks shifting to high binding energy were possibly attributable to the fact that Ti atoms lose partial electrons when $Ti_3C_2T_x$ reduces the intermediate product of $Ni(OH)_2$. As shown in Fig. 3c, the Ni 2p spectra of $Ni/Ti_3C_2T_x$ was well fitted with two spin-orbit doublets related to Ni, Ni-F, and shake-up satellites (denoted as Sat.) [24]. The binding energy of Ni are 852.8 eV in Ni $2p_{3/2}$ spin-orbit level, and 870.34 eV in Ni $2p_{1/2}$ spin-orbit level, respectively. The peak at 856.8 eV corresponding to Ni-F in Ni $2p_{3/2}$ is 0.6 eV lower than the reported data [25], which was ascribed to that the electron of Ni atom was partially transferred to F atom, generating positively charged nickel center [26]. The obtained positive valence of nickel is lower than Ni^{2+}, little different from Ni-F of NiF_2. This result is consistent with the spectra of F 1s (Fig. 3d) whose peak at 684.6 eV of Ni-F is 0.1 eV higher than the reported article [27]. The reason why Ni atom was bonding with F atom rather than O atom is that the bond formation enthalpy of Ni-F is 430 kJ/mol, higher than that of Ni—O (382 kJ/mol), and the dissociation energy of chemical bond of Ni—F (439.7 kJ/mol) is greater than Ni-O (366 kJ/mol), revealing that Ni-F is more stable than Ni-O [28]. In Fig. 3e, the spectra of C 1s could be well deconvoluted into six peaks situated at 282, 282.3, 284.8, 286.3, 288.1 and 292.73 eV which belong to C—Ti—T_x, Ti—C—O, C—C, C—O, O=C—O and C—F bonds, respectively [23,29]. In Fig. 3f, there exist four deconvolution peaks in the spectra of O 1s, demonstrating the four components of Al_2O_3, H_2O and the bond of C-Ti-$(OH)_x$, C-Ti-O_x [30].

The test of N_2 adsorption and desorption was done to grasp the specific surface area of $Ni/Ti_3C_2T_x$, $Ti_3C_2T_x$ and Ti_3AlC_2, presented in Figs. S2a-f (Supporting information). The N_2 adsorption-desorption isotherms of these three kinds of materials were in accordance with IV curves of IUPAC. The specific surface area of $Ni/Ti_3C_2T_x$ (51.282 m^2/g) was larger than that of $Ti_3C_2T_x$ (14.59 m^2/g) and Ti_3AlC_2 (4.726 m^2/g), as a result of the growth of Ni nanoparticles enlarging the interlayered spacing of $Ti_3C_2T_x$, which is in line with XRD patterns. The density functional theory (DFT) pore size distribution of them (Figs. S2b, d and f) mainly appeared in 2.5~6 nm, manifesting the existence of mesopores. The pore volume of $Ni/Ti_3C_2T_x$, $Ti_3C_2T_x$ and Ti_3AlC_2 are 0.063 cm^3/g, 0.027 cm^3/g and 0.007 cm^3/g, respectively, implying that Ni/

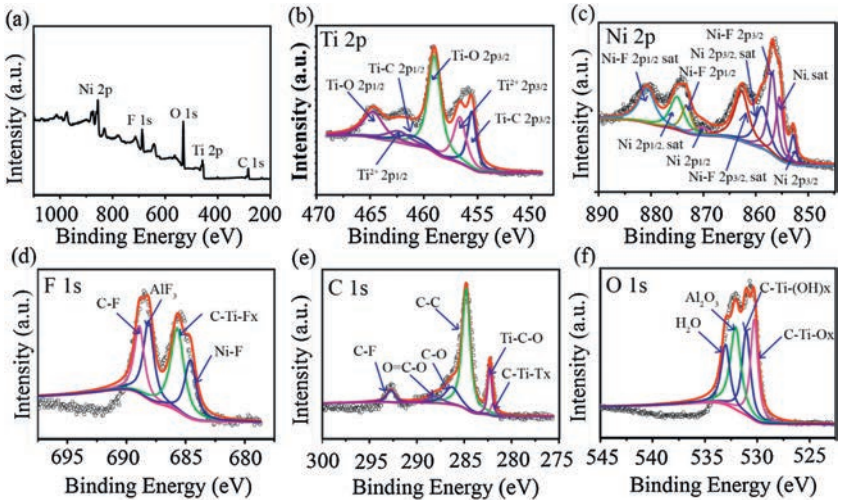

Fig. 3. XPS survey spectrum of (a) Ni/$Ti_3C_2T_x$ hybrid, high-resolution XPS spectra of (b) Ti 2p, (c) Ni 2p, (d) F 1s (e) C 1s, (f) O 1s of Ni/$Ti_3C_2T_x$ hybrid.

$Ti_3C_2T_x$ is more suitable for the accommodation of discharge product.

MXene is a new 2D material with excellent electronic conductivity, structure stability, excellent oxidation resistance and potential high surface area which is conducive to oxygen adsorption and discharge product of lithium-oxygen battery to stick. Ni has been proved to lower the charge overpotential of Li-O_2 battery. Therefore, Ni/$Ti_3C_2T_x$ hybrid is predicted to be an excellent Li-O_2 battery cathode material. With the aim of exploring the electrochemical working mechanism of Ni/$Ti_3C_2T_x$ as cathode of Li-O_2 battery, the related electrochemical tests were carried out. From the Fig. 4a, we can see that even at high current density of 500 mA/g, Ni/$Ti_3C_2T_x$ electrode delivers high discharge capacity of 10,699 mAh/g at first cycle, due to the fact that the high surface area of Ni/$Ti_3C_2T_x$ provides more space to store discharge product. In the second and third round, the specific capacity still can achieve 8635 mAh/g and 3421 mAh/g. The decrease of specific capacity at different circles can be explained by the difficulty of the discharge product decomposing at high current density, so that a fresh cathode cannot be provided. Compared with Ni/$Ti_3C_2T_x$, pure KB has worse specific capacity performance whose discharge specific capacity at first cycle is only 7719 mAh/g, shown in Fig. S3a (Supporting information). As can be seen in Fig. 4b, Ni/$Ti_3C_2T_x$ cathode can stably cycle for 38 rounds at 100 mA/g with the high limited specific capacity of 500 mAh/g. Improving the current density to 500 mA/g, the battery can cycle for 26 rounds. Even if under the presence of catalysis, discharge product can not fully decompose in the charge process, so that Li_2O_2, Li_2CO_3 and LiOH would continuously accumulate on the cathode, which resulted in the cut-off discharge voltage of battery decreasing from 2.75 V to 2.3 V along with the decrease of cycle rounds.

Fig. 4c presents the contrast of the discharge capacity of KB, $Ti_3C_2T_x$ and Ni/$Ti_3C_2T_x$ in various current density at initial round. At 100 mA/g, the discharge specific capacity of Ni/$Ti_3C_2T_x$ (20,264 mAh/g) is much higher than that of KB (7719 mAh/g) and $Ti_3C_2T_x$ (9333 mAh/g). Even at the high current density of 500 mA/g, Ni/$Ti_3C_2T_x$ with nanosized Ni exerting the strong catalytic effect still remained the high discharge capacity of 10,699 mAh/g. Only 2767 mAh/g and 3900 mAh/g can be reached by pure KB and $Ti_3C_2T_x$ at 500 mA/g, respectively. In addition, in

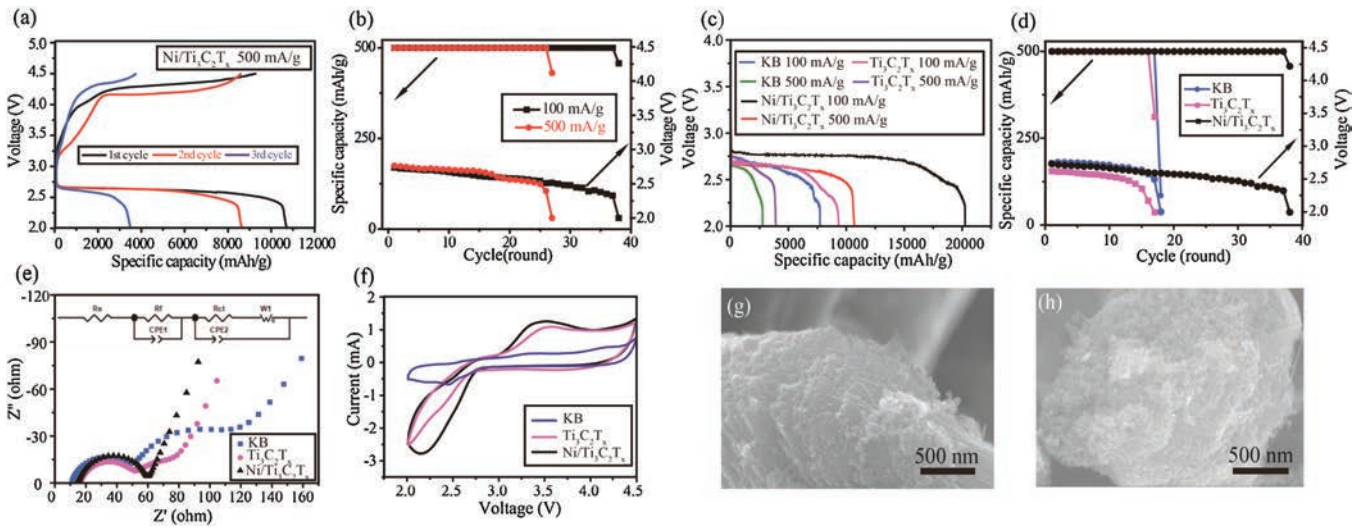

Fig. 4. Electrochemical performance of KB, $Ti_3C_2T_x$ and Ni/$Ti_3C_2T_x$ cathode for lithium-oxygen battery. (a) Discharge and charge curves of full specific capacity of Ni/$Ti_3C_2T_x$ at 500 mA/g. (b) Discharge termination voltage and cycle rounds of Ni/$Ti_3C_2T_x$ at 100 mA/g and 500 mA/g. (c) The comparison of KB, $Ti_3C_2T_x$ and Ni/$Ti_3C_2T_x$ on the first cycle of discharge specific capacity. (d) The comparison of KB, $Ti_3C_2T_x$ and Ni/$Ti_3C_2T_x$ on discharge termination voltage and cycle rounds at 100 mA/g. (e) Nyquist plots of KB, $Ti_3C_2T_x$ and Ni/$Ti_3C_2T_x$. (f) CV curves of KB, $Ti_3C_2T_x$ and Ni/$Ti_3C_2T_x$ with sweep rate of 5 mV/s. SEM images of (g) first discharge product and (h) first charge product.

terms of cycling stability, the cycle numbers of Ni/$Ti_3C_2T_x$ cathode are more than twice that of pure KB and $Ti_3C_2T_x$, illustrated in Fig. 4d. The better performance of Ni/$Ti_3C_2T_x$ hybrid is derived from the increasing attachment sites for the discharge product provided by $Ti_3C_2T_x$ with enhanced electronic conductivity, and catalytic activity site stem from nanosized Ni, preventing the electrochemical reaction from terminating.

Fig. S4a (Supporting information) is the discharge and charge curves of first round at 100 mA/g and 500 mA/g of Ni/$Ti_3C_2T_x$. Benefiting from the excellent electronic conductivity of Ti_3C_2 MXene, the charge overpotential of Ni/$Ti_3C_2T_x$ hybrid at 100 mA/g is 710 mV, lower than that of Ni/KB [31] and $Ti_3C_2T_x$ (1.273 V, Fig. S4b in Supporting information), attributed to the interaction of Ni and $Ti_3C_2T_x$. At 500 mA/g, the charge overpotential increased to 1.14 V, perhaps ascribed to the internal electrode resistance [32]. Conversely, the charge overpotiental of pure KB (Fig. S3b in Supporting information) is 1.02 V, higher than that of Ni/$Ti_3C_2T_x$ (710 mV), because of Ni/$Ti_3C_2T_x$ electrode combining one advantage of facilitating decomposition of discharge products Li_2O_2 and another advantage of the high stable structure of $Ti_3C_2T_x$. Moreover, the cycle stability of Ni/$Ti_3C_2T_x$ cathode is proved by the discharge and charge curves in different rounds at 100 mA/g and 500 mA/g, exhibited in Figs. S4c and d (Supporting information). The discharge voltage plateau of 100 mA/g stabilized at 2.73 V at the first 20 rounds and decreased to 2.6 V after long-time cycling because of the accumulation of undecomposed discharge product covering active sites of Ni/$Ti_3C_2T_x$ cathode. However, Ni/$Ti_3C_2T_x$ cathode exhibited worse cycling performance at 500 mA/g whose discharge voltage plateau stabilized at 2.7 V, owing to the lower kinetic reaction rate and difficult decomposition of discharge product.

Electrochemical impedance spectroscopy (EIS) test aims to deeply investigate the electrochemical performance of Ni/$Ti_3C_2T_x$ hybrid. The Nyquist plots of KB, $Ti_3C_2T_x$ and Ni/$Ti_3C_2T_x$ hybrid before cycling can be seen from Fig. 4e. The semicircle at high frequency is associated with the diffusion of Li^+ through SEI film on the surface of active material, while the semicircle at medium frequency is related to the charge transfer process and the slope line at low frequency could be utilized to study Warburg diffusion impedance [33,34]. There are two semicircles of KB and $Ti_3C_2T_x$ obviously appearing in high and medium frequency area. However, the Ni/$Ti_3C_2T_x$ visibly possesses one semicircle at medium and high frequency. The Nyquist plots could be specifically analyzed by means of simulating the equivalent circuit diagram, illustrated in Fig. 4e. And the fitted datas are detailedly enumerated in Table S2 (Supporting information). It can be seen from the data in Table S2 that the resistance of the electrolyte (expressed in R_s) of KB is lower than that of $Ti_3C_2T_x$ and Ni/$Ti_3C_2T_x$ hybrid. The interface SEI resistance (written as R_f) and the charge transfer impedance (represented as R_{ct}) of $Ti_3C_2T_x$ are 35.48 Ω and 33.4 Ω, respectively, less than 40.54 Ω and 69.22 Ω of KB, separately, suggesting that $Ti_3C_2T_x$ can improve electronic conductivity of the cathode. What is more, the value of the combination of R_f (2.887 Ω) and R_{ct} (42.19 Ω) of Ni/$Ti_3C_2T_x$ are the smallest, confirming that Ni/$Ti_3C_2T_x$ makes contributions to enhancing catalytic activity and stability of the Li-O_2 battery cathode [34]. Comparison of the fitting data reveals that Ni/$Ti_3C_2T_x$ could efficiently heighten electrochemical reaction kinetics of the cathode.

In order to find out electrochemical catalytic effect of Ni/$Ti_3C_2T_x$ in lithium-oxygen battery, cyclic voltammetry (CV) tests are implemented in Fig. 4f. The onset reduction potential and peak current as well as the oxidation peak current of Ni/$Ti_3C_2T_x$ are higher than those of pure KB and $Ti_3C_2T_x$, respectively, suggesting that Ni/$Ti_3C_2T_x$ contributes to higher ORR activity and better OER catalytic activity. Two apparent OER peaks at lower potential and higher potential for Ni/$Ti_3C_2T_x$ can be seen in Fig. 4f, which are associated with the deintercalation of outer part of Li_2O_2 and the oxidation of most Li_2O_2 [35,36]. The morphology of discharge product Li_2O_2 is like thin slice [37], shown in Fig. 4g. After charging, flaky Li_2O_2 broke down, leading to no thin sheet in Fig. 4h.

To sum up, Ni/$Ti_3C_2T_x$ hybrid was synthesized through hydrothermal along with calcination. Layer structure of MXene with Ni distributing uniformly on the interlayer and surface of $Ti_3C_2T_x$, was not destroyed after keeping at high temperature in the protected gas Ar. The Ni/$Ti_3C_2T_x$ hybrid serving as cathode catalyst for Li-O_2 battery delivers high discharge specific capacity (20,264 mAh/g at 100 mA/g and 10,699 mAh/g at 500 mA/g) and stable cycle performance maintaining 38 rounds at 100 mA/g. The high surface area and excellent electronic conductivity of MXene and outstanding catalytic activity of Ni make Ni/$Ti_3C_2T_x$ a suitable cathode catalyst for lithium-oxygen battery. This work provides a promising strategy to design MXene-based nanomaterials applied in Li-O_2 battery cathode.

Acknowledgment

This work was supported by the National Natural Science Foundations of China (Nos. 21871028, 21471020 and 21771024).

Appendix A. Supplementary data

Supplementary material related to this article can be found, in the online version, at doi:https://doi.org/10.1016/j.cclet.2019.09.028.

References

[1] G. Girishkumar, B. McCloskey, A.C. Luntz, S. Swanson, W. Wilcke, J. Phy. Chem. Lett. 1 (2010) 2193–2203.
[2] L. Grande, E. Paillard, J. Hassoun, et al., Adv. Mater. 27 (2015) 784–800.
[3] J. Lu, L. Li, J.B. Park, et al., Chem. Rev. 114 (2014) 5611–5640.
[4] L. Wang, Y. Zhang, Z. Liu, L. Guo, Z. Peng, Green Energy Environ. 2 (2017) 186–203.
[5] C. Liu, R. Younesi, C.W. Tai, et al., J. Mater. Chem. A Mater. Energy Sustain. 4 (2016) 9767–9773.
[6] M.M.O. Thotiyl, S.A. Freunberger, Z. Peng, P.G. Bruce, J. Am. Chem. Soc. 135 (2013) 494–500.
[7] M.M.O. Thotiyl, S.A. Freunberger, Z. Peng, et al., Nat. Mater. 12 (2013) 1049–1055.
[8] C. Wang, Z. Xie, Z. Zhou, Appl. Mater. 7 (2019) 040701.
[9] N.K. Chaudhari, H. Jin, B. Kim, et al., J. Mater. Chem. A Mater. Energy Sustain. 5 (2017) 24564–24579.
[10] M. Naguib, V.N. Mochalin, M.W. Barsoum, Y. Gogotsi, Adv. Mater. 26 (2014) 992–1005.
[11] V.M.H. Ng, H. Huang, K. Zhou, et al., J. Mater. Chem. A Mater. Energy Sustain. 5 (2017) 3039–3068.
[12] Y.T. Liu, P. Zhang, N. Sun, et al., Adv. Mater. 30 (2018) 1707334.
[13] L. Yu, L. Hu, B. Anasori, et al., ACS Energy Lett. 3 (2018) 1597–1603.
[14] Q. Zhao, Q. Zhu, J. Miao, P. Zhang, B. Xu, Nanoscale 11 (2019) 8442–8448.
[15] X. Zhang, Z. Zhang, Z. Zhou, J. Energy Chem. 27 (2018) 73–85.
[16] D. Ji, S. Peng, D. Safanama, et al., Chem. Mater. 29 (2017) 1665–1675.
[17] M.W. Yuan, R. Wang, W.B. Fu, et al., ACS Appl. Mat. Interfaces 11 (2019) 11403–11413.
[18] M. Yuan, C. Nan, Y. Yang, et al., ACS Omega 2 (2017) 4269–4277.
[19] M. Yuan, L. Lin, Y. Yang, et al., Nanotechnology 28 (2017) 185401.
[20] M. Yuan, Y. Yang, C. Nan, et al., Appl. Surf. Sci. 444 (2018) 312–319.
[21] Z. Liu, N. Feng, Z. Shen, et al., ChemSusChem 10 (2017) 2714–2719.
[22] Y.J. Oh, J.H. Kim, S.K. Park, et al., Chem. Eng. J. 351 (2018) 886–896.
[23] J. Yan, C.E. Ren, K. Maleski, et al., Adv. Funct. Mater. 27 (2017) 1701264.
[24] A.P. Grosvenor, M.C. Biesinger, R.S.C. Smart, N.S. McIntyre, Surf. Sci. 600 (2006) 1771–1779.
[25] M. Jin, G. Zhang, F. Yu, et al., Phys. Chem. Chem. Phys. 15 (2013) 1601–1605.
[26] H. Zhang, L. Yu, T. Chen, W. Zhou, X.W. Lou, Adv. Funct. Mater. 28 (2018) 1807086.
[27] H. Han, J. Woo, Y.R. Hong, Y.C. Chung, S. Mhin, ACS Appl. Energy Mater. 2 (2019) 3999–4007.
[28] Y.M. Lee, K.M. Nam, E.H. Hwang, et al., J. Phys. Chem. C 118 (2014) 10631–10639.
[29] A. Rozmyslowska-Wojciechowska, E. Karwowska, S. Pozniak, et al., RSC Adv. 9 (2019) 4092–4105.
[30] J. Halim, K.M. Cook, M. Naguib, et al., Appl. Surf. Sci. 362 (2016) 406–417.
[31] C. Wang, Y. Zhao, J. Liu, et al., Chem. Commun. 52 (2016) 11772–11774.
[32] Z. Hou, J. Long, C. Shu, et al., J. Alloys. Compd. 798 (2019) 560–567.
[33] X. Yang, L. Zhang, F. Zhang, Y. Huang, Y. Chen, ACS Nano 8 (2014) 5208–5215.
[34] K. Zhang, Y. Xu, Y. Lu, et al., J. Mater. Chem. A Mater. Energy Sustain. 4 (2016) 6404–6410.
[35] T. Zhu, X. Li, Y. Zhang, et al., J. Electroanal. Chem. 823 (2018) 73–79.
[36] X. Li, T. Zhu, C. Wen, et al., Electrochim. Acta 317 (2019) 367–374.
[37] Z. Sun, M. Yuan, L. Lin, et al., ACS Appl. Energy Mater. 2 (2019) 4144–4150.